

NICMOS images of the GG Tau Circumbinary Disk

C. McCabe, G. Duchêne & A.M. Ghez

Department of Physics and Astronomy, University of California, Los Angeles

mccabe@astro.ucla.edu

ABSTRACT

We present deep, near-infrared images of the circumbinary disk surrounding the pre-main-sequence binary star, GG Tau A, obtained with NICMOS aboard the Hubble Space Telescope. The spatially resolved proto-planetary disk scatters $\sim 1.5\%$ of the stellar flux, with a near-to-far side flux ratio of ~ 1.4 , independent of wavelength, and colors that are comparable to the central source ($\Delta(M_{F110W} - M_{F160W}) = 0.10 \pm 0.03$, $\Delta(M_{F160W} - M_{F205W}) = -0.04 \pm 0.06$); all of these properties are significantly different from the earlier ground-based observations. New Monte Carlo scattering simulations of the disk emphasize that the general properties of the disk, such as disk flux, near side to far side flux ratio and integrated colors, can be approximately reproduced using ISM-like dust grains, without the presence of either circumstellar disks or large dust grains, as had previously been suggested. A single parameter phase function is fitted to the observed azimuthal variation in disk flux, providing a lower limit on the median grain size of $a > 0.23 \mu\text{m}$. Our analysis, in comparison to previous simulations, shows that the major limitation to the study of grain growth in T Tauri disk systems through scattered light lies in the uncertain ISM dust grain properties. Without explicit determination of the scattering properties it is not possible to differentiate between geometric, scattering and evolutionary effects. Finally, we use the 9 year baseline of astrometric measurements of the binary to solve the complete orbit, assuming that the binary is coplanar with the circumbinary ring. We find that the estimated 1σ range on disk inner edge to semi-major axis ratio, $3.2 < R_{in}/a < 6.7$, is larger than that estimated by previous SPH simulations of binary-disk interactions.

Subject headings: binaries:close—ISM:dust—scattering—stars:individual (GG Tau)—stars:pre-main sequence—planetary systems:proto-planetary disks

1. Introduction

GG Tau A is one of the few T Tauri systems in which a disk has been spatially resolved at both millimeter and near-infrared wavelengths and is therefore an ideal system for detailed studies of proto-planetary disk geometry and composition. As the second brightest millimeter object in the survey of Beckwith et al. (1990), GG Tau was an early target for millimeter wave interferometry studies (Simon & Guilloteau 1992; Kawabe et al. 1993; Dutrey, Guilloteau & Simon 1994; Guilloteau, Dutrey & Simon 1999, hereafter G99). These observations showed the emission to be from a massive ($0.13M_{\odot}$) disk surrounding GG Tau A, the closest pair of stars in the GG Tau quadruple stellar system¹, with the bulk of the emission arising from a distinct ring structure extending from 180 to 260 AU (assuming a distance of 139 pc; Bertout, Robichon & Arenou, 1999). The circumbinary disk was subsequently detected via near-infrared scattered light in multi-wavelength, ground-based adaptive optics (AO) images (Roddier et al. 1996, hereafter known as R96) and in space-based Hubble Space Telescope (HST) 1 μm polarimetric images (Silber et al. 2000) and WFPC2 optical images (Krist, Stapelfeldt & Watson 2002).

Analysis of the ground-based near-infrared images resulted in disk colors that appear to be redder than the central stars (R96). Such a red color excess could either indicate that the circumbinary disk has a substantial population of large dust grains, or that circumstellar disks, which are coplanar with the circumbinary disk, redden the stellar light before it scatters off the circumbinary disk. Comparing the variation of disk magnitude with color around the disk, Roddier et al. find a trend for fainter regions of the disk to be redder, leading them to suggest that circumstellar disks are the cause of the observed red color excess. The existence of circumstellar disks around the individual components in GG Tau A is supported by observations of near-infrared excesses and strong hydrogen emission lines in each component (White et al. 1999). No information, however, is currently available regarding their orientation and in fact many disks in binary systems show evidence of non-coplanarity (e.g., Stapelfeldt et al. 1998; Monin, Ménard & Duchêne, 1998; Jensen et al. 2000; Wood et al. 2001). To test the circumstellar disk hypothesis, Wood, Crosas & Ghez (1999) ran Monte Carlo scattering simulations of the GG Tau circumbinary ring with and without circumstellar disks being present. Using the Kim, Martin & Hendry (1994) interstellar medium (ISM) grain properties and the disk geometry derived by Dutrey et al. (1994), they find that the circumstellar disks are required to match the disk to star flux ratios and near side to far side flux ratios observed in the ground-based AO images. While these simulations roughly reproduce the estimated quantities due to the large observational uncertainties, they predict

¹GG Tau A-B, Aa-b and Ba-b are separated by $10''$, $0''.25$ and $1''.48$ respectively (Leinert et al. 1991).

blue rather than red disk color excesses. In order to make further progress in understanding the role of circumstellar disks and the possibility of large particles, much higher signal to noise measurements of the circumbinary disk are required at multiple wavelengths.

In this paper we present new high angular resolution, multi-wavelength observations of the GG Tau system taken with NICMOS aboard HST. These deep, space-based observations offer a more stable point spread function (PSF) than that obtainable with ground-based AO systems, allowing a more accurate determination of the disk properties. The observations are outlined in §2 and the data reduction and PSF subtraction method used are explained in §3. Newly derived stellar and circumbinary disk properties are presented in §4 and are discussed in sections §5 and §6 in light of additional Monte Carlo simulations.

2. Observations

GG Tau A ($\alpha = 04^h32^m30^s.3$, $\delta = +17^\circ31'41''$, $J2000$) was observed using the near-infrared camera, NICMOS, aboard HST on 1997 October 10. Deep images were obtained with the F110W ($\lambda_o = 1.03\mu\text{m}$, $\Delta\lambda = 0.55\mu\text{m}$), F160W ($\lambda_o = 1.55\mu\text{m}$, $\Delta\lambda = 0.40\mu\text{m}$), and F205W ($\lambda_o = 1.90\mu\text{m}$, $\Delta\lambda = 0.60\mu\text{m}$) filters². In the F110W and F160W filters, GG Tau was imaged 9 times on NIC1, the NICMOS camera with the smallest field of view, $11'' \times 11''$, and pixel scale of $0.''043$ per pixel (Thompson 1995). Each image was offset by $2.''2$ in a spiral dither pattern in order to reduce residual flat field uncertainties and the dither size was set to a non-integral number in order to reduce intra-pixel sensitivity variations, while also keeping the circumbinary disk in the field of view. Each individual dither image was integrated for 128 seconds in the multiaccum mode. The F205W filter data were taken using NIC2, which has a $19.''2 \times 19.''2$ field of view and a pixel scale of $0.''075$ per pixel. Due to the significant thermal background at this wavelength a dither-chop observing pattern was employed, whereby each image is composed of one 128 second integration on GG Tau followed by a $32''$ chop and a 128 second integration on a blank piece of sky. Nine images were obtained in this manner.

Because the aim of our research was to detect faint, diffuse emission close to bright sources, a good characterization of the point spread function was required. To this end, images of a calibrator star, NTTS 042417+1744, were obtained in the same manner as GG Tau in each of the above mentioned filters. This weak-lined T Tauri star has a number

²The NICMOS F110W and F160W filters correspond well to the standard ground-based J and H band filters, with the F160W filter providing the closest match. The F205W filter is centered $\sim 0.3 \mu\text{m}$ shorter than the standard K band filter and is $\sim 0.2 \mu\text{m}$ wider.

of properties which were used to select it as a calibrator: no infrared excess indicative of circumstellar material (Walter et al. 1988), known to be single from previous speckle interferometry observations (Ghez et al. 1993), only half a magnitude brighter than GG Tau Aa in the J band ($1.25 \mu\text{m}$), and a spectral type of K1, which is similar to the stellar components of the binary star (K7 and M0.5 for GG Tau Aa and Ab respectively; White et al. 1999).

3. Data Analysis

3.1. Image Processing

Initial data reduction was carried out by STScI, providing a quick analysis of the data quality. The images were recalibrated with the latest calibration reference files using the STScI’s pipeline routine CALNICA (Bushouse, Skinner & MacKenty, 1996), which performs standard image reduction tasks: removal of bias and dark current levels, interpolation over known bad pixels, flatfielding, and removal of all cosmic ray hits. Once the data were calibrated, each individual image was sub-pixelated by a factor of 2.

In order to obtain estimates of the properties of the central binary (§4.1) and the circumbinary disk (§4.2), a model of the central binary star was generated through PSF fitting and then subtracted from the individual images. Both the empirical PSF (observations of NTTS 042417+1744) and TinyTim model PSFs (Krist, 1993) were used. The PSF-fitting was carried out for each of the nine GG Tau images by minimizing the chi-squared between the PSF model and the data in the regions dominated by the binary star (the central area of $\sim 0.67 \text{ arcsec}^2$) and, in the case of the empirical PSF, the diffraction spikes (an additional $\sim 1.65 \text{ arcsec}^2$ comprising 4 rectangular regions covering the diffraction spikes beyond $2''$ distance from the central binary). For the empirical PSF, all nine PSF estimates were evaluated and the one that produced the best fit, i.e., the smallest residuals, was selected for each GG Tau image. Although the TinyTim routine allowed us to match the colors of the two GG Tau A stellar components as well as the focus position of the observations (see §3.2), the empirical PSF models consistently produced smaller residuals than those created using TinyTim, and thus the final values for the central binary and the circumbinary disk were derived using the empirical PSF model subtracted images. The difference in the quality of the fits between the empirical PSF and the TinyTim PSF can be understood in terms of (a) small scale PSF variations due to the telescopes “breathing”, the change in the focus of the telescope on timescales of an orbit due to a varying thermal load, and (b) the presence of scattered light off the telescope optics (Krist and Hook, 1999). Neither of these effects are incorporated into the TinyTim PSF models used, and both are measured with the empirical

PSF. The nine model subtracted images were combined together to form an average subtracted image at each wavelength, which are shown in Figure 1. Azimuthal averages of the model subtracted images are plotted in the first row of Figure 2.

3.2. Bias and Uncertainty Estimates

3.2.1. Measurement Uncertainties

A map of the measurement uncertainties was created by taking the standard deviation of the mean from all nine PSF subtracted images of GG Tau. Azimuthal averages of these statistical uncertainties are shown in the second row of Figure 2; while these values provide a good estimate of the uncertainties associated with the measurement and subtraction process, they do not take into account the presence of any systematic effects.

3.2.2. Systematic Biases and Associated Uncertainties

Two systematic effects that alter the structure of the PSF have been identified. The first, which affects all three band passes, arises because the observed PSF, NTTS 042417+1744, is slightly bluer than either component of GG Tau. The second is an inadvertent focus offset between the object and PSF in the F205W data. These effects create a systematic bias and an additional source of uncertainty, both of which were modeled and accounted for.

In order to investigate the consequences of the small color differences between the object and PSF, we generated polychromatic models of GG Tau Aa, Ab and NTTS 042417+1744 using TinyTim, matching the spectral shape of these objects using previous photometry from Ghez et al. (1997) and Walter et al. (1988). The PSF fitting and subtraction process was run on the TinyTim model images in order to produce a model of the bias term (i.e., the subtraction residuals caused by this color mismatch); azimuthal averages of this color bias are plotted in the first row of Figure 2. To obtain an estimate of the uncertainty associated with this measurement of the color bias, the method was repeated using a PSF that varied in spectral type by the assumed uncertainty in the calibrators spectral type (one subclass). The difference in residuals between using a PSF of spectral type K0 and K1 is our estimate of the statistical uncertainty on the color bias term (plotted in the second row of Figure 2); the uncertainty on the color bias is significantly smaller than the measurement uncertainties.

While this method was sufficient for the F110W and F160W data, the F205W data required an additional systematic effect to be accounted for. Observations of GG Tau on

NIC2 were run in parallel mode with polarization observations (which are not presented here) on NIC1. Due to the unexpected thermal problems, each NICMOS camera had a different optimal focus position and therefore parallel observations were taken at non-optimal focus positions. Since these observations were scheduled prior to the recognition of this problem, the polarization data were arbitrarily regarded as the prime observation. Therefore both the polarization and F205W observations were made with the NIC1 focus setting, resulting in slightly out of focus F205W observations. Unfortunately, the F205W data on the PSF were taken in a separate orbit with no parallel observations and therefore at the optimal NIC2 focus setting. This mismatch in focus between the object and calibrator in the F205W data set was quantified using the same TinyTim modeling used to determine the color bias in the F110W and F160W data, but incorporating both the color difference and mean focus offset. As shown in the third column of Figure 2, the focus bias is the source of a considerably large systematic error. To estimate the systematic uncertainty associated with the measurement of this bias, a polychromatic TinyTim model of GG Tau was created with the focus set at the *maximum* focus position of the data set, and then subtracted using a K0 type PSF set at the *mean* focus position of the PSF data set. As focus and color mismatches can cause similar problems, this model set-up maximizes the difference between the PSF for the object and calibrator data sets. In contrast with the F110W and F160W data sets, the uncertainty associated with the bias term in the F205W data dominates the measurement uncertainties.

3.2.3. Combining Statistical and Systematic Effects

All of the results presented in §4 are obtained from analysis of images that have had estimates of the systematic bias subtracted out and uncertainties that have been combined in quadrature, as described in equations 1 and 2.

$$Final_{\lambda} = Img_{\lambda} - Bias_{\lambda} \tag{1}$$

$$\sigma_{\lambda}^{TOT} = \sqrt{(\sigma_{\lambda}^{img})^2 + (\sigma_{\lambda}^{bias})^2} \tag{2}$$

Img_{λ} is the median of the nine PSF subtracted images and $Bias_{\lambda}$ is the systematic bias from the mismatch in color and focus position. The two error terms in equation 2 are the statistical uncertainties of the image measurement and bias modeling respectively. The final row in Figure 2 displays the azimuthally average of the bias corrected signal-to-noise (e.g., $Final_{\lambda}/\sigma_{\lambda}^{TOT}$). Analysis of the F205W dataset is limited to the measurement of the binary star properties (§4.1) and integrated disk photometry (§4.2.2), since it is significantly affected

by the focus bias. Although this bias and its associated uncertainty have been modeled, the models were made using TinyTim PSFs that have been shown to deviate somewhat from the observed PSFs.

4. Results

In this section we present the observed properties of the stellar system and the circumbinary disk. The binary orbital motion has been followed for the past 9 years and the newly estimated disk mass and inclination (G99) allow us to derive estimates of all the orbital parameters for the binary system using only minimal assumptions (§4.1). For the circumbinary disk (§4.2), we focus on the following observational quantities that have, in the past, been considered useful tools in comparing observations and disk models: in §4.2.1, the disk morphology (Wood et al. 1999), in §4.2.2, the disk to star flux ratio (Wood et al. 1999) and color excesses (R96), and in §4.2.3, the spatially resolved color-magnitude relationships (R96) and near side to far side flux ratios (Close et al. 1998; Wood et al. 1999). These properties are then compared to earlier measurements. Deviations from previous estimates of these quantities are most likely attributable to a combination of low SNR and over-deconvolution of the disk in the more challenging AO observations.

4.1. Central Binary Star Properties

Table 1 lists the values for the binary separation, position angle (P.A.) and magnitude of each component obtained from the PSF fitting of the central binary star. The uncertainties are the standard deviation of the estimates obtained from the nine individual measurements, plus additional contributions from the uncertainties of the spacecraft orientation ($0^{\circ}03$; Holtzmann et al., 1995a) and the pixel scale (0.5%; NICMOS Instrument Handbook). The 5% uncertainty in the absolute photometry calibration, however, is not included as our analysis rests on the relative photometry of the disk compared to the central stars. The reported individual stellar flux density uncertainties are dominated by PSF variations. Wide aperture photometry was carried out with the assumption that the disk is a small contamination on the stellar light ($\sim 1\%$, see §4.2.2); this both checks the PSF fitting measurements and provides a more precise value of the total stellar flux which is used in §4.2.2. Using an aperture $2''.6$ in radius, we obtain a total binary flux density that is consistent to within 1σ with the values found through PSF fitting (see Table 1).

Over the 9 year period 1990 to 1998, the binary system was repeatedly observed (Leinert

et al. 1993; Ghez et al. 1995, 1997; Roddier et al. 1996; Silber et al. 2000; White & Ghez 2001; Woitas, Köhler & Leinert 2001; Krist et al. 2002). Both the new HST photometric and astrometric measurements agree well with the other reported measurements. Furthermore, the astrometric collection of measurements has grown significantly such that estimates of the relative velocities in the plane of the sky can be greatly improved. Combining the HST measurements with those published previously³ and assuming constant linear motion, we find a velocity of $6.68 \pm 0.52 \text{ mas yr}^{-1}$ at a position angle of $260^\circ \pm 5^\circ$, with an average relative position of $0''.2485 \pm 0''.0013$ at the position angle of $358^\circ.2 \pm 0^\circ.3$. This velocity has a factor of 5 smaller uncertainties than previous estimates (Ghez et al. 1995; Woitas et al. 2001), mostly resulting from including more measurements. With the greater precision in both the velocity reported here and the total mass of the system, derived from the rotation of the circumbinary disk (G99), it is now possible to solve for the whole orbit, assuming only that the orbit is coplanar with the circumbinary ring, and that the ring is intrinsically circular. Appendix A provides the details of how the orbital parameters, e , a , P , T_0 , ω and their uncertainties are derived from the observables, \vec{r}_{2D} , \vec{v}_{2D} , M , i , D , Ω .

We find that the stars are in an elliptic orbit with an eccentricity $e = 0.32 \pm 0.20$ and a semi-major axis $a = 35_{-8}^{+22}$ AU. The corresponding orbital period is 185_{-55}^{+195} yr. We emphasize that the uncertainties quoted here include the uncertainty on the distance to the Taurus molecular cloud, which must also be taken into account when considering the system mass (G99). Indeed, together with the uncertainty in the measured velocity, this is the dominant source of error in the quoted uncertainties. Although the orbital parameters derived here still have large uncertainties, this analysis shows the applicability of this method. Additional astrometric data over the next few years should help to significantly decrease these uncertainties and ascertain the exact orbit of the binary. We note that our orbital solution differs significantly from that obtained in the past, in the sense that we find that the stars are close to apoastron while R96 concluded that the stars must be close periastron. This contradiction is the result of our estimated velocity being much smaller than the earlier estimate, and smaller than the velocity one would observe if the orbit was circular. A similar conclusion, based on velocity comparison alone, was recently reached by Krist et al. (2002). Our derived orbit is shown in Figure 3, where we have also plotted yearly weighted averages of the data points used in the fit.

In the framework of investigating interactions between the ring and the inner binary, it

³Average uncertainties have been assigned to all measurements obtained with the same method. As a result, decreasing weights are assigned to HST ($\sigma_r = 2.5mas$), speckle interferometry ($\sigma_r = 5mas$) and adaptive optics ($\sigma_r = 10mas$) astrometric results, respectively. Furthermore, the astrometry from Leinert et al. (1993), obtained from three separate 1D measurements is not included in our fit.

is interesting to compare the inner radius of the circumbinary disk to the semi-major axis of the system. The ratio of these two quantities lies in a 1σ range $3.2 < R_{in}/a < 6.7$; the two stars have cleared a wide gap around them. Artymowicz & Lubow (1994) have used analytical and numerical approaches to study the formation of such a gap through gravitational resonances in geometrically thin disks around circular and eccentric binary systems. The orbital properties of GG Tau A provide us with the first direct test of these models in pre-main-sequence visual binary systems, although uncertainties prevent us from reaching definitive conclusions. Artymowicz & Lubow found that this gap clearing phenomenon is primarily driven by the orbital eccentricity, with a smaller dependence on the mass ratio, ($M_B/M_A \sim 0.9$ in the case of GG Tau A; White et al. 1999). The results of Artymowicz & Lubow can be summarized as follows: while the R_{in}/a ratio is on the order of 1.7 for circular orbits, it can grow up to ~ 3.3 for highly eccentric binaries ($e = 0.75$). The derived orbital parameters appear somewhat problematic, with a R_{in}/a ratio that seems to be larger than those expected for a moderately eccentric system. This may mean that the dynamical evolution of the GG Tau circumbinary ring is more complex than previously thought.

4.2. Circumbinary Disk Properties

4.2.1. Disk Detection & Morphology

Azimuthal averages of the PSF subtracted images (see Figure 2) show that the circumbinary disk is easily detected at radii greater than $\sim 1''$ at all three wavelengths. The circumbinary disk is detected with an average SNR > 5 per pixel at radii of $0''.9$ to $\sim 1''.9$ (F110W and F160W) and $1''.1$ to $1''.9$ (F205W data) with an average peak surface brightness of 15.3, 14.1 and 14 mag/arcsec² in F110W, F160W and F205W respectively. At smaller radii the 1σ subtraction noise level rises dramatically, from ~ 14 mag/arcsec² at $0''.5$ to ~ 11 mag/arcsec² at $0''.2$, with each filter having a slightly different noise level (see Figure 2). This prevents a meaningful investigation of gap material that has been posited in varying forms in earlier observations (R96; Silber et al. 2000; Krist et al. 2002).

A model of the two-dimensional near-infrared apparent disk geometry is constructed from the F110W and F160W data by analyzing the intensity profile of the disk as a function of azimuth. Note that what we are observing here is the geometry of the optically thick scattered light distribution, not the true disk geometry. For every 10 degree segment of the disk, an average radial profile is produced. The position of the radial profile peak value is found using two methods. The first calculates a weighted centroid over a $0''.5$ region centered on the maximum value of the radial profile, which works well on sections of the disk that have a distinct peak. The south side of the disk, however, has a much flatter radial profile,

and the weighted centroid method is not as stable for these segments. The second method fits the radial profile with a 4 degree polynomial. The ‘center’ of the disk is then calculated by finding the midpoint between the two radii at which the disk value is equal to half the peak value. For the north side of the disk where the radial profile is almost gaussian in shape, this method finds the same disk peak. For the flatter southern profiles it provides a more robust method of finding the disk center. The final peak position values are taken from the results of the polynomial fit. This method of finding the disk peak location also provides an estimate of the width of the radial profile, which is taken to be the distance between the two half-peak radii. Uncertainties for these values are estimated by taking the largest of either the difference between the values found through the two methods or the standard deviation of the values found from applying the same analysis to 3 subsets of the data.

The overall apparent shape of the disk is explored by fitting an ellipse to the positions of the radial profile peak values. We find an ellipse with a semi-major axis of $1''.42 \pm 0''.06$ (200 AU) orientated at a position angle, PA_{NIR} of $21^\circ \pm 9^\circ$ and an eccentricity of 0.64 ± 0.02 . Although only G99 provided uncertainties for their analysis, our measurements of the ring geometry are consistent with that found in both the previous near-infrared (R96) and millimeter observations (Dutrey et al. 1994; G99). If you assume that the disk is intrinsically circular and geometrically thin, the observed eccentricity corresponds to a disk inclination of $40^\circ \pm 2^\circ$. While this is consistent with inclination measurements made from the optically thin millimeter images of the circumbinary ring ($i = 37^\circ \pm 1^\circ$, $PA_{disk} = 7^\circ \pm 2^\circ$; G99), the disk is known to be geometrically thick, which should bias the observed inclination towards slightly larger values. G99 also note that the geometrical thickness of the inclined ring will cause the northern inner edge of the scattered light ring to appear closer to the center of mass of the system than the inner edge observed in the optically thin millimeter images. This offset can be used to calculate the total height of the disk above the midplane, i.e., where the NIR light becomes optically thin. This height is where the disk is physically truncated in the Monte Carlo simulations (see §5). In the NICMOS images, the northern inner edge (the peak of the radial profile) occurs $0''.88 \pm 0''.07$ away from the center of mass. From the disk model fits to the millimeter images (G99), the inner edge of the millimeter disk occurs at a projected distance of $R \cos i = 1''.03 \pm 0''.02$. The offset, $0''.15 \pm 0''.07$, corresponds to a total disk height of 35_{-18}^{+21} AU (using the relation from G99). This is smaller than the $0''.25$ offset derived by G99 from the deconvolved adaptive optics images of R96. In addition, the disk height will also translate into an offset between the center of the ring and the center of mass of the system. The disk fitting routine finds that the center of the ring is offset from the center of mass of the binary by $0''.21 \pm 0''.03$ along a position angle of $162^\circ \pm 9^\circ$ degrees, consistent with the offset measured from the inner edge.

The width of the disk has a clear azimuthal dependence, with the North side being

narrower than the South side, as noted by both Silber et al. (2000) and Krist et al. (2002). Figure 4 shows the measured width, which ranges from $0''.3$ to $\sim 1''$, as a function of position angle. We fit these measurements with a modified Henyey-Greenstein scattering phase function (described in §4.2.3), which is physically meaningless in this context but provides an analytical description of the data. This analysis shows that the thinnest portion of the disk occurs at a position angle of 356° , independent of wavelength (see Table 2). Because the function we used for the fit is unphysical and provides only a moderately good fit, we do not estimate uncertainties.

At the lowest contour levels we observe a deviation away from the elliptical fit along the southern edge of the disk (see Figure 5). This deviation consists of a sharp elbow, or kink, in the south-east edge of the disk and a straightening of the isophotes along the southern edge which makes the disk outer edge appear boxy. This effect is present in all 3 filters, and coincides with the kink detected by Silber et al. (2000) and noted by Krist et al. (2002).

4.2.2. *Integrated Disk Photometry*

In order to assign flux densities to the disk, we define an annular aperture with an eccentricity of 0.64 centered at the position of the center of the ellipse with an inner semi-major axis at $1''$ and outer semi-major axis at $2''.2$, based on the results given in §4.2.1. The area affected by the diffraction spikes is particularly noisy and is excluded from the aperture by masking off these regions, reducing the effective aperture area from 9.2 to 5.82 square arcseconds. The spike mask comprises two diagonal stripes, $0''.8$ in width, centered on the position of the primary. Summing the counts over this area and correcting the flux for the masked off regions (by multiplying the area of the masked regions with the mean disk flux per pixel), provides the estimates of the total disk magnitudes given in Table 1. Since the pixel scale is smaller than the diffraction limit, the estimated uncertainties are based on maps that have been averaged over regions corresponding to the diffraction limited beam sizes ($0''.1$, $0''.16$ and $0''.2$ for F110W, F160W and F205W respectively). These measurements of the integrated disk intensity have an order of magnitude higher signal to noise ratios than earlier ground-based measurements.

The overall disk magnitudes are compared to those derived for the binary system (§4.1) to obtain disk to star flux ratios and color excesses (see Table 3). The NICMOS images presented here lead to a disk to star flux ratio of $\sim 1.5\%$, which is 2.5 times larger than that derived by R96. Likewise, the color of the circumbinary disk is comparable to that of the stars:

$$\begin{aligned}\Delta(M_{F110W} - M_{F160W}) &= 0.10 \pm 0.03 \\ \Delta(M_{F160W} - M_{F205W}) &= -0.04 \pm 0.06\end{aligned}$$

where $\Delta(M_1 - M_2)$ is the color excess of the disk, or $(M_1 - M_2)_{disk} - (M_1 - M_2)_{star}$. This is in contrast to the large red excess suggested earlier.

4.2.3. Spatially Resolved Disk Photometry

The spatially resolved color properties of the circumbinary disk are investigated by calculating the disk magnitudes within circular apertures which are $0''.19$ in diameter (roughly the size of the $2 \mu\text{m}$ diffraction limit) placed around the disk. For this comparative analysis, the F110W and F160W bias-subtracted images have been convolved to the resolution of the F205W image. Only areas of the disk used to calculate the integrated disk photometry are included in this analysis. Figure 6 displays the resulting color-magnitude plot, which shows no significant trend in color with respect to magnitude. Unlike the results from R96, the NICMOS measurements provide no evidence for extinction within the disk.

As originally mentioned by R96, the disk exhibits azimuthal variations in intensity that are presumed to arise from angular variations in the scattering efficiency, with the brightest side of the ring corresponding to forward scattering from the edge of the disk that is nearest to our line of sight. Here we present a detailed quantitative analysis of these azimuthal variations, using normalized peak flux densities derived from the 10° azimuthal averages discussed in §4.2.1. To estimate the position angle of the brightest region, the data are fit, using a chi-square minimization technique, with a modified⁴ form of the Henyey-Greenstein scattering phase function (Henyey & Greenstein, 1941)

$$S(PA) \propto [1 - g'^2][1 + g'^2 - 2g' \cos(PA - PA_0)]^{-3/2}$$

where PA_0 is the value of position angle that maximizes the function. While the use of this function is not physically meaningful, as the phase function depends on scattering angle, not position angle on the sky, it does provide a convenient method of characterization. The best-fit functions are displayed with the data in the left hand column of Figure 7 while the values

⁴The following two small modifications have been made to the Henyey-Greenstein scattering phase function for fitting the position angle of the brightest region: (1) the albedo, which normally is included as a multiplicative factor, is omitted, since we have normalized the data and (2) the position angle of the brightest region, PA_0 , is added.

of PA_0 and the fitted peak-to-peak near side to far side flux ratios are listed in Table 2. The peak near side to far side flux ratio is ~ 4 with no significant wavelength dependence. The position angle of the brightest portion of the disk ($22^\circ \pm 4^\circ$) is roughly consistent with that measured by Krist et al. (2002) in I band images (25°) and both the position angle of the semi-minor axis ($7^\circ \pm 2^\circ$, G99) and the position angle of the thinnest region (-4° , derived in §4.2.1). This provides strong support for the hypothesis that the disk is geometrically thick.

The azimuthal variations in intensity arise from variations in dust grain scattering efficiencies as a function of scattering angle, rather than the observed position angle around the disk. Assuming a single scattering scenario in a geometrically thin disk, Close et al. (1998) derive scattering properties of the dust grain population by matching the intensity extrema to scattering angles of $90 - i$ and $90 + i$, which, with an assumed inclination, i , of 35° , results in scattering angles of 55° and 125° . The NICMOS images, however, contain much more information than just the intensity extrema, as the circumbinary disk samples a large range of scattering angles as a function of position angle around the disk. We therefore take the additional step of fitting the entire azimuthal variation of flux with a scattering phase function. Using the known disk geometry, the observed variation with position angle can be translated, or de-projected, into a variation with scattering angle, θ , which is defined as the angle of deflection away from the forward direction of the incoming light. θ is geometrically related to the position angle around the disk, PA , the position angle which maximizes the azimuthal variation, PA_0 , and the disk inclination, i , by:

$$\cos(\theta + \phi_{open}) = \sqrt{1 - \frac{1}{1 + \cos^2(PA - PA_0)\tan^2(i)}} \times (-1)^j$$

where

$$\begin{aligned} j &= 1 \text{ if } \cos(PA) < 0 \\ j &= 0 \text{ if } \cos(PA) > 0 \end{aligned}$$

A derivation of this relation can be found in Appendix B. ϕ_{open} is the opening angle of the disk as seen from the stars; including this factor converts the relation from a geometrically thin disk to a thick disk case. It is assumed here that, at all position angles on the sky, the intensity is dominated by the portion of the ring corresponding to the smallest scattering angle, which is true for forward-scattering grains. Using the values for the inner radius of the disk and a disk height of 35 AU, we calculate ϕ_{open} to be 11° . In this case, with an inclination of 37° , the scattering angle ranges from $\sim 40^\circ$ at the closest edge to $\sim 120^\circ$ at the edge furthest from us. Using the above relationship to translate the observed position angle

into scattering angles, the intensity variations are then fitted with a normalized Henyey-Greenstein scattering phase function, in order to estimate the value of the dust asymmetry parameter, g . This parameter is the averaged cosine of the scattering angle which ranges in value from -1 to 1. Given that we are using the one parameter Henyey-Greenstein scattering phase function we can only investigate forward throwing dust grains with $0 < g < 1$. In this case, if the light is scattered isotropically, then the amount of forward scattered light equals that being back-scattered and $g=0$. As the light becomes more strongly forward-scattered, the value of g increases. The results of the fit for the dust asymmetry are summarized in Table 2. We find that omitting the disk opening angle will slightly overestimate g . It should be recalled that these values are obtained under the assumption of single scattering (see §5.2 for further discussion).

Since the system may be modulated by geometric factors, such as a possible shadowing by circumstellar disks, Wood et al. (1999) found it more convenient to work with an integrated quantity to describe the near side to far side flux ratio. Integrating the flux over the northern and southern halves of the disk, as defined by the position angle of the disk, we find the ratio of scattered light to be ~ 1.4 , with no significant wavelength dependence (see Table 3). This value is roughly a factor of two smaller than that seen in the ground-based AO images (Wood et al. 1999).

5. Discussion

In this section, we use the various quantities derived in §4 to revisit the question of whether the existence of large dust grains or opaque circumstellar disks are required to explain the observed color excesses. Monte Carlo scattering simulations are presented, qualitatively reproducing the NICMOS data (§5.1) and emphasizing the key role played by grain properties, especially the dust asymmetry (§5.2). The scattering simulations show that neither circumstellar disks or large grains are absolutely needed to reproduce the data and that our fitted scattering phase function can be used to derive a lower limit on the median size of the scatterers.

5.1. Numerical Modeling of the GG Tau Ring

Since the NICMOS measurements of the GG Tau circumbinary disk provide different results from both those previously reported and modeled, we ran new Monte Carlo simulations to investigate whether the observed disk colors can be reproduced using a standard

ISM grain model. We began, like Wood et al. (1999), with the simplest case: modeling the scattered light distribution from a thick torus of ISM-like dust, without the additional complications of either circumstellar disks or grain growth (their model 1).

We used a Monte Carlo code that was readily available to us; the same model which successfully reproduced the NICMOS polarization results (Silber et al. 2000). The Monte Carlo code is based on a program from Ménard (1990) that has been modified such that each photon interacts with a randomly sampled dust grain from the input grain size distribution. Details of the modifications can be found in Duchêne (1999). The disk is modeled as a thick torus, using a total disk height of 38 AU at the inner edge of the ring, close to that estimated from the observed inner edge offset (see §4.2.1). This torus has a total disk mass of $0.13 M_{\odot}$ and a scale height of 21 AU at the inner edge of the ring (180 AU) that varies as $r^{1.05}$ (G99). Outcoming photons are sorted by inclination: all results presented here are for the range of inclinations closest to the actual inclination of the system, $37^{\circ} < i < 46^{\circ}$. The simulations follow 1 million photons per filter. The dust grain properties are taken from the Mathis & Whiffen (1989, hereafter known as MW) dust model. While the dust parameters (e.g., albedo and dust asymmetry) in the MW dust model differ significantly from the Kim, Martin & Hendry (1994; hereafter known as KMH) model⁵ used by Wood et al. (1999), both models successfully reproduce the ISM extinction curve. The simulated disk properties can be found in Table 3. The resulting Monte Carlo simulations (see model 1 in Table 3) roughly recreate the observed disk to star flux ratios and near side to far side flux ratios. They also produce a considerably red disk color excess, $\Delta(M_{F110W} - M_{F160W}) = 0.50$, $\Delta(M_{F160W} - M_{F205W}) = 0.28$. This is distinctly larger than the color excess observed with NICMOS, and very different from the blue scattered light disk seen in the Wood et al. (1999) models.

The two main differences between the Wood et al. simulations and those presented here are the dust grain properties used⁶ and a slightly different disk geometry. Both the overall disk height and the degree of flaring differ (Wood et al. use a scale height that varies as

⁵MW dust grains are composite and porous in nature, composed of silicate, graphite, amorphous carbon and vacuum. The grain size distribution follows $n(a) \propto a^{-3.7}$ between 0.03 and 0.9 μm (MW model A for an $R_V = 3.1$). In contrast, the KMH dust grains are composed of separate silicate and graphite particle populations, with a size distribution of $n(a) \propto a^{-3.5} \exp(-a/0.2\mu\text{m})$ between 0.005 and 1 μm .

⁶Note that there is also a slight difference in the way the dust parameters are calculated. Wood et al. calculate the mean dust parameters for the grain population and assign these to each dust particle, whereas the dust parameters for each photon-dust particle interaction in the simulations presented here are calculated on the fly after the grain size has been randomly sampled from the grain size distribution. While this method is more computationally expensive, we believe it to be more representative of the actual phenomenon. How large an effect this difference makes has not been investigated so far.

$r^{1.25}$ from the earlier millimeter work of Dutrey et al. 1994). To fully compare our numerical results with those of Wood et al., we ran Monte Carlo simulations where the only difference is the dust grain properties. The results from these simulations (see model 2 in Table 3) show that the red disk color excesses remain and therefore are predominantly caused by the dust grain properties.

5.2. The Influence of Multiple Scattering and Grain Properties: Explaining the Different Modeled Colors

The apparently contradictory simulations presented here and in Wood et al. can be reconciled by investigating the effect the different dust grain properties have on the scattering process. In optically thick situations, photons are scattered multiple times. The resulting scattered light surface brightness is dependent on two key dust parameters, the albedo of the dust, ω , and the azimuthal scattering dependence given by the dust asymmetry parameter, g . In terms of disk geometry, the inclination of the system is also an important factor. At any one scattering angle, the output scattered surface brightness is dependent on both the albedo of the dust and the number of scattering events n , such that $SB_{scat} \propto \omega^{n(g\lambda)}$ (e.g., Witt & Oshel, 1977; Witt 1985). The greater the number of scatterings, which is a function of the dust asymmetry parameter, the greater reduction in the resulting scattered surface brightness.

The simulations presented here and those in Wood et al. (1999) are based on the same Monte Carlo scheme and have the same disk geometry. The main difference lies in grain properties used, and this alone is enough to explain the disk color reversal between the two sets of models. Table 4 compares the dust properties used in the two simulations. The dust asymmetry of the median scatterer in our simulations is ~ 2 times larger than that used by Wood et al., while the albedos are essentially the same. How does this affect the observed scattered light distribution? Consider first the far side (southern edge) of the ring where back-scattering is the dominant effect. For low g values, such as those used in the Wood et al. simulations, the scattering is not far from being isotropic, which means that the photons leaving the disk toward the line of sight will in general have gone through a small number of scatterings (~ 1). Thus the resulting surface brightness distribution will not be strongly affected by multiple scattering effects and the scattered light colors will be similar to the wavelength dependence of the dust albedo, resulting in Wood et al.’s case in blue disk color excesses. For more strongly forward scattering dust particles (large g), back-scattering is rarer and in this region of the disk most of the scattering events will cause photons to move further into the disk, away from our line of sight. The photons that do

escape from the surface of the disk toward our line of sight will have undergone a much larger number of scatterings and the resulting scattered light surface brightness will be significantly changed by the wavelength dependence of the dust asymmetry parameter. For the MW dust properties, not only is g larger than those in the KMH model, they also have a stronger wavelength dependence. The scattered light surface brightness will be more reduced at $1 \mu\text{m}$ than it is at $2 \mu\text{m}$ producing significantly red disk colors. The same story applies to the nearest (northern) edge of the disk, where we are predominantly seeing forward scattering off the upper limb of the ring. This type of scattering is enabled by both low and high g values (near-isotropic and strongly forward scattering); while the number of scattering events remains small in both simulations there will still be more scattering events for the photons in our simulation than those in Wood et al.’s due to the inclination of the system favoring low g values slightly more. This, combined with the corresponding slightly longer pathlength in our simulation, enabling more extinction, is enough of an effect to compensate for the intrinsically blue color of the scattering, as seen in our simulations. Taking the disk as a whole, this explains why our simulations predict a red disk color, while those of Wood et al., being dominated by the flux from the far side of the disk, result in overall blue disk colors. The same $\omega^{n(g\lambda)}$ dependency is responsible for the reduced disk to star flux ratios and increased near to far flux ratios observed in our simulations, as photons undergo more scattering events in the far side of the disk than in Wood et al.’s (see Table 3). Given the range of colors that can be simulated using the two grain models, it could be expected that a grain population with properties intermediate of those in the KMH and MW models would result in neutral near-infrared colors, as observed.

An additional effect of multiple scattering observed in our simulations is that the disk inclination and optical thickness combine to modify the azimuthal intensity variation from that expected from single scattering. Given that the observed surface brightness is dominated by the least scattered photons (ω^n dependency), for grains that are predominantly forward-scattering, photons received from the back side of the ring are biased towards the back scattering part of the phase function. Statistically, most of the photons will be scattered towards the middle of the ring and will either not reach the observer or be of an extremely low intensity. Scattering from the front edge of the ring, however, will remain mostly unbiased. This biasing effect will cause the derived g value measured in §4.2.3 to underestimate the true dust asymmetry, and hence our value is only a lower limit. The same reasoning applies to the Close et al.’s analysis, as a consequence of considering only single scattering. As an example of this effect, in our simulations, the size of the median scattering grain is $0.56 \mu\text{m}$ and these have an asymmetry parameter $g \sim 0.8$ at $1 \mu\text{m}$. However, the measured g from the simulations (obtained using the same method as in §4.2.3) is only ~ 0.3 .

The observed lower limit on g , measured in §4.2.3 provides a lower limit on the median

size of the scatterers as the asymmetry value is a sensitive function of the size parameter, $x (= 2\pi a/\lambda)$, for g less than ~ 0.8 . From the MW grain properties used, we find that the measured asymmetry of $g > 0.39$ at $1 \mu\text{m}$ corresponds to a grain size, $a > 0.23 \mu\text{m}$.

6. Implications and Summary

The GG Tau disk is clearly detected ($SNR_{pix} > 5$) in all three NICMOS filters between radii of $1''.0$ to $2''.2$, scattering approximately 1.5% of the stellar light. No discernible wavelength dependence of scattered light is observed, although azimuthal variations in both width and intensity are seen and modeled. We confirm the observation of a kink in the disk by Silber et al. (2000). Observed as a sharp elbow in the disk on the south-east edge, followed by a flattening of the isophotes along the southern edge of a disk, this feature is seen in all three filters. The projected distance of the northern edge from the center of mass, related to the total height of the ring, provides the first hint that the ring may not be as thick as previously estimated, with a total height of 35 AU at the inner edge of the disk (180 AU).

The presence of such a well-observed circumbinary ring around this system, combined with the 9 year baseline of binary observations has allowed us to constrain the orbital parameters of the binary. We find a slightly elliptical orbit $e = 0.3 \pm 0.2$, with a semi-major axis $a = 35^{+22}_{-8}$ AU and a corresponding orbital period of 185^{+195}_{-55} yr. The 1σ range of estimated orbital semi-major axis is such that the ratio of semi-major axis to inner disk radius is larger than expected from previous SPH simulations (Artymowicz & Lubow, 1994). This suggests that the dynamical evolution of the circumbinary ring may be more complex than previously thought. Further astrometric observations of this close binary are needed to constrain the binary orbit further.

The Monte Carlo simulations summarized in §5.1 show the wide range of colors one can ‘predict’ from the GG Tau disk, from blue to red, using different dust size distributions and grain properties (ω, g). Specifically, our Monte Carlo simulations show that the observed neutral disk colors, ratio of disk to star light, and near side to far side flux ratio can probably be reproduced with some combination of an ISM-like grain size distribution and dust properties and does not necessarily require either the presence of large dust grains or prior extinction by circumstellar disks. However, this does not rule out that either is present. Because the disk is optically thick in the near-infrared, studies of scattered light are only sensitive to those grains that are located near the surface of the ring. Any conclusion about grain growth only applies to those regions and does not provide any information the size of grains deep in the ring. For instance, it has been shown that grains larger than $\sim 1 \mu\text{m}$ tend to segregate in the disk midplane because of their larger mass (e.g., Suttner & Yorke 2001)

and possibly as the result of the enhanced grain-grain collision rate in higher density regions. The presence of such large grains in the midplane cannot be determined in our near-infrared observations. Circumstellar disks are known to surround both components of GG Tau A, however, the possible effects they have on the integrated circumbinary disk colors have been shown to be subtle and somewhat surprising. While Krist et al. (2002) suggest that the red disk colors observed in the optical could be caused by an $A_V \geq 1.2$ mag of extinction, possibly in the form of circumstellar disks, Wood et al. (1999) find that the inclusion of small circumstellar disks can actually cause the integrated disk colors to become *bluer* rather than redder. Analysis of the disk colors at both optical and near-infrared wavelengths is planned for future work.

While the color of scattered light in optically thick disks cannot currently be used to constrain grain properties, the azimuthal intensity variations can be used to provide a lower limit on the median grain size, independent of grain model. This lower limit ($g > 0.39$ at $1 \mu\text{m}$) corresponds to a median grain size of $a > 0.23 \mu\text{m}$. Given that the ISM dust models produce a wide range of median grain sizes ranging from $\sim 0.16 \mu\text{m}$ (Mathis, Rumpl & Nordsieck 1977; KMH) to $0.56 \mu\text{m}$ (MW), this lower limit does not suggest that grain growth has occurred in the surface layers of the disk in this young (~ 1 Myr old; White et al. 1999) system.

There is still considerable uncertainty regarding the ISM dust properties (e.g., Witt 2000), a point which is well illustrated here by the comparison of Monte Carlo scattering results using two of the more well known dust grain models. Both the KMH and MW grain models, like most of the ISM dust models to date, have been constrained using the ISM extinction curve, which they reproduce equally well. The results presented here suggest that using the extinction curve *alone* to constrain the dust properties introduces a significant level of uncertainty in the scattering properties of the grains. As an example, KMH and MW grain models predict V band g 's of ~ 0.5 and ~ 0.9 respectively. Observations of reflection nebulae in the same bandpass infer $g \sim 0.7$, significantly different from either of these models (Witt, Oliveri & Schild, 1990). Additionally, models of T Tauri disks seen in scattered light with WFPC2 find that the observations are best fit by $g \sim 0.65$ (Burrows et al. 1996; Stapelfeldt et al. 1998; Krist et al. 2002), although these values may be affected by grain growth. Combining additional sources of information, such as observations of dust scattering (e.g., Witt, et al. 1990), polarization (e.g., Zubko & Laor 2000), and dust thermal emission (e.g., Li & Draine 2001) will provide additional constraints. Without a more detailed knowledge of the ISM dust grain properties it is unlikely that we will be able to unambiguously determine whether grain growth is occurring in T Tauri disks through scattered light imaging.

Although dust properties in the disk cannot currently be constrained from either colors

or dust asymmetry alone, this work provides an outline for future analysis and modeling. Observationally, further resolved intensity and polarization maps at other wavelengths are key in sampling a large enough grain size parameter (x) range to constrain the dust grain properties. For instance, at 3 to 5 μm the dust asymmetry is expected to be much more isotropic, allowing significant color variations (e.g., $J - L$) between the front and back sides, unless significant grain growth has already occurred. Such observations should be carried out in parallel with a full exploration of the parameter space (grain size distribution, grain properties, ring geometry) through Monte Carlo scattering simulations.

The authors thank Mike Jura, Alycia Weinberger, François Ménard, Kenny Woods, Lisa Prato, and Angelle Tanner for enlightening discussions. We also thank the anonymous referee for their constructive comments. Support for this work was provided by NASA through grant number GO-06735.01-95A from the Space Telescope Institute, the NASA AstroBiology Institute and the Packard Foundation. This research was based on observations made with the NASA/ESA Hubble Space Telescope, obtained at the Space Telescope Science Institute, which is operated by the Association of Universities for Research in Astronomy, Inc, under NASA contract NAS5-26555. This research has made use of the SIMBAD database, operated at CDS, Strasbourg, France.

A. Determination of the orbital parameters of the binary

In this appendix, we present the method used to derive the orbital parameters of the binary from a single measurement of its separation and relative velocity with some additional knowledge available from previous studies.

The orbit of a binary system can be described with a set of 9 independent parameters: mass ratio (q), eccentricity (e), total mass (M), orbital period (P), time of periastron (T_0), inclination of the orbital plane (i), position angle on the sky of the ascending node of the orbit (Ω), angle in the orbital plane between periastron and the ascending node (ω), and distance to the system (D). Note also that P and M are linked to the semi-major axis of the orbit, a , through Kepler’s third law. When considering the *relative* motion of one component around the other one, q is no longer a relevant parameter. Therefore, one must measure 8 independent quantities to solve the orbit unambiguously. In the case of GG Tau, the millimeter interferometric measurement of the circumbinary ring by G99 yields precise estimates of three independent parameters: the inclination of the ring, $i' = 37^\circ \pm 1^\circ$, the position angle of the apparent semi-minor axis of the ring, $\Omega' = 7^\circ \pm 2^\circ$, and the total system mass $M = 1.28 \pm 0.07 \times (D/140 \text{ pc})M_\odot$. If the ring is intrinsically circular then $\Omega = \Omega' \pm 90^\circ$ (depending on the motion of the binary). Furthermore, if we assume that

the orbital plane corresponds to the ring mid-plane, we have $i = i'$. These two assumptions (circular ring and coplanar orbit) are the only assumptions we make in the following analysis. Additionally, the HIPPARCOS determination of the distance to the Taurus star-forming region, $D = 139 \pm 10$ pc, by Bertout et al. (1999), allows us to convert the apparent separation and velocity of the binary into absolute values. Prior to our work, the problem could thus be simplified to a problem with only four unknowns.

The orbit of the system has been followed over the last ten years or so and, since all measurements so far are consistent with a uniform linear motion, we combined them all to obtain the average binary separation and linear velocity projected on the sky. These quantities can be represented for instance by the respective amplitude of the binary separation and of its velocity (ρ and $\dot{\rho}$, measured in arcsec and arcsec.yr⁻¹) and by the angle between these two vectors in the plane of the sky (δ). In the following derivation, a useful quantity is the angle θ between the apparent semi-minor axis of the ring and the binary separation, which represents the polar coordinate of the current measurement with respect to the disk itself. This angle can be expressed as $\theta = \Omega' - PA_{bin}$. Our data imply $\rho = 0''.2485 \pm 0''.0013$, $\dot{\rho} = (6.68 \pm 0.52) 10^{-3}$ ''yr⁻¹, $\delta = 96^\circ.0 \pm 5^\circ.5$ and $\theta = 11^\circ.2 \pm 2^\circ.1$ (see §4.1). The orientation of the relative velocity implies that $\Omega = 97^\circ$. We have thus obtained the four last measurements needed to solve the whole orbit.

The two-body problem is a classical mechanics problem, the solution of which can be found in many textbooks. We are interested here in the case where only relative measurements of the 3D binary separation (\vec{r}) and velocity (\vec{v}) are available from the de-projection of the observed separation and motion in the orbital plane. The eccentricity and semi-major axis can then be derived from measurements of the angular momentum, $j = |\vec{r} \times \vec{v}|$, and total energy, $E = \frac{1}{2}v^2 - \frac{GM}{r}$, *per unit mass*. We have the following relations: $e^2 = 1 + \frac{2j^2 E}{G^2 M^2}$ and $a = -\frac{GM}{2E}$. These relations can be translated into the observables presented above as follows:

$$e^2 = 1 + \frac{\rho^2 \dot{\rho}^2 D^4 \sin^2 \delta}{G^2 M^2 \cos^2 i} \left\{ \dot{\rho}^2 D^2 \left[\sin^2(\delta + \theta) + \frac{\cos^2(\delta + \theta)}{\cos^2 i} \right] - 2 \frac{GM \cos i}{\rho D} \right\}$$

and

$$a = GM \left\{ 2 \frac{GM \cos i}{\rho D} - \dot{\rho}^2 D^2 \left[\sin^2(\delta + \theta) + \frac{\cos^2(\delta + \theta)}{\cos^2 i} \right] \right\}^{-1}$$

One can immediately derive the orbital period: $P(\text{yr}) = \sqrt{\frac{a^3(\text{AU})}{M(M_\odot)}}$. Uncertainties for all of these quantities were obtained by allowing all seven observables to vary within 1σ of their nominal value and retaining the extreme values for each orbital parameter. Special care must be taken when considering the uncertainties induced by the distance estimate, as the total mass of the system is also affected in a *systematic* manner by the distance. The

distance and relative velocity of the binary estimates combine for the largest part of the total uncertainty for the orbital elements.

For completeness, we derive the remaining two orbital parameters that have not been addressed so far, ω and T_0 . The former is the angle, in the orbital plane, between periastron and the ascending node. This can be derived from the angular distance between the current location of the companion and periastron. The latter angle can be determined using the general equation of the elliptical orbit,

$$r = \frac{a(1 - e^2)}{1 + e \cos(\phi - \varpi)}$$

where r and ϕ are the polar coordinates of a point running along the orbit and ϖ is the position angle of periastron. Using the current de-projected separation of the system, 43.0 AU, we find that the binary is about $(\phi - \varpi) = -145^\circ$ away from periastron⁷. Combining this information with the angle between the current binary location and the ascending node (100°), we conclude that $\omega = 245^\circ$. To estimate how much time it takes for the companion to go from one point to another along the orbit, we use Kepler’s second law and numerically integrate the area A defined by the section of an ellipse between these two points. We can easily calculate the time derivative of the area, which is related to the angular momentum per unit mass by $\frac{dA}{dt} = \frac{1}{2}j$. Applying this to the average position of the companion and periastron, we find that the next periastron passage will occur about 61 yrs from now or, equivalently, that $T_0 = 2472467$ JD. Both ω and T_0 depend heavily on the previously derived quantities, therefore, we emphasize that the uncertainties on these parameters are rather large.

B. Calculating Scattering Angles

In this section we derive a relation between position angle around a disk and the angle a photon is scattered through. At each position angle around the disk, we assume that the observed photons are scattered off the closest disk edge which corresponds to the smallest available scattering angle (see §4.2.3).

Consider a circular ring that is inclined to the line of sight at an angle i . This ring is projected on the sky as an ellipse (see Figure 8a), with normalized semi-major axis, $d = 1$ and aspect ratio $c/d = \cos i$. The position angle on the sky of a random point around the disk, PA , is defined as $\tan(PA) = x/y$. In Figure 8a we have rotated the image so that the

⁷The negative sign reflects the fact that the binary is slowly getting tighter, hence closer to periastron.

semi-minor axis of the disk is now vertical. The amount of rotation, PA_0 , is the PA of the semi-minor axis of the disk, defined in the usual manner.

The scattering angle is defined as the angle between the pre- and post- scattering directions, \vec{n} and \vec{m} respectively, as shown in Figure 8b. This angle, θ_{scat} , is $\theta - \phi_{open}$, where ϕ_{open} is the angle subtended by the disk height. If the disk can be assumed to be flat, we have $\theta_{scat} = \theta$. We first consider this case before generalizing our results to $\phi_{open} \neq 0$. The coordinates of the unit vector \vec{n} , (u, v, w) are along the photon's initial path to a random point on the ring, $M(x, y)$, in the $(\vec{x}, \vec{y}, \vec{z})$ frame are:

$$u = x \tag{B1}$$

$$v = y \tag{B2}$$

$$w = \sqrt{(1 - x^2 - y^2)} \times \text{sign}(\cos(PA)) \tag{B3}$$

Writing the standard equation of an ellipse:

$$\left(\frac{x}{d}\right)^2 + \left(\frac{y}{c}\right)^2 = 1$$

and introducing the definitions of i and PA , we find:

$$x^2 \left(1 + \frac{1}{\tan^2(PA)\cos^2(i)}\right) = 1$$

By definition, the dot product of the unit vectors, \vec{n} and \vec{m} is:

$$\vec{n} \cdot \vec{m} = \begin{pmatrix} 0 \\ 0 \\ 1 \end{pmatrix} \cdot \begin{pmatrix} u \\ v \\ w \end{pmatrix} = \cos(\theta)$$

$$\cos(\theta) = \sqrt{(1 - x^2 - y^2)} \times \text{sign}(\cos(PA)) \tag{B4}$$

$$\cos(\theta) = \sqrt{1 - x^2 \left(1 + \frac{1}{\tan^2(PA)}\right)} \times \text{sign}(\cos(PA)) \tag{B5}$$

$$\cos^2(\theta) = 1 - \frac{x^2}{\sin^2(PA)} \tag{B6}$$

$$\tag{B7}$$

Substituting the expression for x^2 :

$$1 - \cos^2(\theta) = \frac{1}{\sin^2(PA) \left(1 + \frac{1}{\tan^2(PA) \cos^2 i}\right)} \quad (\text{B8})$$

$$= \frac{1}{1 + \cos^2(PA) \left(\frac{1}{\cos^2 i} - 1\right)} \quad (\text{B9})$$

$$= \frac{1}{1 + \cos^2(PA) \tan^2(i)} \quad (\text{B10})$$

$$\cos(\theta) = \sqrt{1 - \frac{1}{1 + \cos^2(PA) \tan^2(i)}} \times \text{sign}(\cos(PA)) \quad (\text{B11})$$

or

$$\cos(\theta) = \sqrt{1 - \frac{1}{1 + \cos^2(PA) \tan^2(i)}} \times (-1)^j$$

where

$$\begin{aligned} j &= 1 \text{ if } \cos(PA) < 0 \\ j &= 0 \text{ if } \cos(PA) > 0 \end{aligned}$$

Reintroducing the position angle on the sky of the semi-minor axis of the ellipse, PA_0 and the disk opening angle, ϕ_{open} , we can generalize this as:

$$\cos(\theta) = \cos(\theta_{scat} + \phi_{open}) = \sqrt{1 - \frac{1}{1 + \cos^2(PA - PA_0) \tan^2(i)}} \times (-1)^j$$

For a face-on disk ($i = 0^\circ$) the scattering angle is always $90^\circ - \phi_{open}$. Note that this relation between scattering angle and disk inclination breaks down for edge-on disks ($i = 90^\circ$).

REFERENCES

- Artymowicz, P., & Lubow, S.H., 1994, ApJ, 421, 651
- Beckwith, S. V. W., Sargent, A. I., Chini, R. S. & Guesten, R., 1990, AJ, 99, 924
- Bertout, C., Robichon, N., & Arenou, F., 1999, A&A, 352, 574
- Bohren & Huffman, 1983, Scattering of Light from Small Particles
- Bushouse, H., Skinner, C., & MacKenty, J., 1996 Instrument Science Report ISR NICMOS-009
- Burrows, A., Stapelfeldt, K., Watson, A., Krist, J.E., Ballester, G.E. et al. 1996, ApJ, 473, 437
- Close, L.M., Dutrey, A.M., Roddier, F., Guilloteau, S., Roddier, C., Duvert, G., Northcott, M., Ménard, F., Graves, J.E. & Potter, D. 1998, ApJ, 499, 883
- Duchêne, G. PhD, Université de Grenoble, 1999
- Dutrey, A., Guilloteau, S., and Simon, M. 1994, A&A, 286, 149
- Ghez, A.M., Neugebauer, G. and Matthews, K. 1993, AJ, 106, 2000
- Ghez, A.M., Weinberger, A.J., Neugebauer, G., Matthews, K., McCarthy, D.W., Jr., 1995, AJ, 110, 753
- Ghez, A.M., White, R. and Simon, M. 1997, ApJ, 490, 353
- Guilloteau, S., Dutrey, A., and Simon, M. 1999, A&A, 348, 570 (**G99**)
- Heney, L.G., & Greenstein, J.L., 1941, ApJ, 93, 70
- Holtzmann, J. A. et al. 1995, PASP, 107, 156
- Jensen, E.L.N., Donar, A. X., & Mathieu, R. D., 2000, IAU Symp. 200, The Formation of Binary Stars, 85
- Kawabe, R., Ishiguro, M., Omodaka, T. Kitamura, Y. & Miyama, S. M. 1993, ApJ, 404, L63
- Kim, S., Martin, P.G., & Hendry, P.D., 1994, ApJ, 422, 164 (**KMH**)
- Krist, J. 1993, A.S.P. Conference Series, Astronomical Data Analysis Software and Systems II, Vol. 2, 536

- Krist, J. & Hook, R.N., 1999, The 1997 HST Calibration Workshop with a New Generation of Instruments, 192
- Krist, J.E., Stapelfeldt, K.R. & Watson, A.M., 2002, ApJ, in press
- Leinert, C., Haas, M., Mundt, R., Richichi, A., & Zinnecker, H., 1991, A&A, 250, 407
- Leinert, C., Zinnecker, H., Weitzel, N., Christou, J., Ridgway, S.T., Jameson, R., Haas, M. & Lenzen, R., 1993, A&A, 278, 129
- Li, A., & Draine, B.T., 2001, ApJ, 554, 778
- Mathis, J.S., Rumpl, W., & Nordsieck, K.H., 1977, ApJ, 217, 425
- Mathis, J.S., & Whiffen, G., 1989, ApJ, 341, 808 (MW)
- Ménard, F. PhD, Université de Montreal, 1990
- Monin, J.-L., Ménard, F., & Duchêne, G., 1998, A&A, 339, 113
- Roddier, C., Roddier, F., Northcott, M.J., Graves, J.E., and Jim, K. 1996, ApJ, 463, 326 (R96)
- Silber, J., Gledhill, T., Duchêne, G., Ménard, F., 2000, ApJ, 536, L89
- Simon, M., & Guilloteau, S., 1992, ApJ, 397, L47
- Stapelfeldt, K.R., Krist, J.E., Ménard, F., Bouvier, J., Padgett, D.L., & Burrows, C.J., 1998, ApJ, 502, L65
- Suttner, G. & Yorke, H.W., 2001, ApJ, 551, 461
- Thompson, R., 1995, Proc. SPIE, 2475, 367
- Walter, F., Brown, A., Mathieu, R.D., Myers, P.C., and Vrba, F.J. 1988, AJ, 96, 297
- White, R.J., Ghez, A.M., Reid, N., Schultz, G. 1999, ApJ, 520, 811
- White, R.J., & Ghez, A.M., 2001, ApJ, 556, 265
- Witt, A.N., & Oshel, E.R., 1977, ApJS, 35, 31
- Witt, A.N., 1985, ApJ, 294, 216
- Witt, A., Oliveri, M.V., & Schild, R.E., 1990, AJ, 99, 888

Witt, A., 2000, IAU Symp. 197, Astrochemistry: From Molecular Clouds to Planetary Systems, 317

Woitas, J., Köhler, R., & Leinert, Ch., 2001, A&A, 369, 249

Wood, K., Crosas, M. & Ghez, A., 1999, ApJ, 516, 335

Wood, K., Smith, D., Whitney, B., Stassun, K, Kenyon, S.J., Wolff, M.J., & Bjorkman, K.S., 2001, ApJ, 561, 299

Zubko, V.G., & Laor, A., 2000, ApJS, 128, 245

Table 1. Stellar and Integrated Circumbinary Disk Results^{ab}

Filter	Separation (arcsecs)	Position Angle (degrees)	Aa (mag)	Ab (mag)	Aa + Ab ^c (mag)	Disk ^d (mag)
F110W	0.248 ± 0.002	353.9 ± 0.4	9.37 ± 0.05	10.27 ± 0.07	8.98 ± 0.02	13.59 ± 0.01
F160W	0.251 ± 0.002	353.8 ± 0.3	8.39 ± 0.01	9.08 ± 0.04	7.91 ± 0.02	12.42 ± 0.01
F205W	0.257 ± 0.003	353.6 ± 0.8	7.94 ± 0.01	8.61 ± 0.01	7.46 ± 0.02	12.01 ± 0.05

^aThe zeropoints used are 1775, 1083 and 731 Jy in F110W, F160W and F205W respectively (M. Rieke, priv. comm).

^bThe reported photometric uncertainties do not include the 5% uncertainty in the zeropoints as the analysis presented here rests on the relative photometry of the disk compared to the central stars.

^cCombined binary magnitude is measured using wide aperture photometry and assuming the disk is a small ($\sim 1\%$) contamination on this.

^dEstimated disk brightness integrated over 9.2 arcsec^2 (see §4.2.2 for details).

Table 2. Azimuthal Variations

	Width ^a		Flux Density		Lower Limit
	Amplitude	PA ^b	Amplitude ^c	PA_0	g
F110W	2.3	-1	4.3 ± 0.7	22 ± 4	0.39 ± 0.02
F160W	3.1	-8	3.1 ± 0.4	19 ± 7	0.30 ± 0.02

^aNo uncertainties are calculated for the fit to the width variation as the fitting function is not sufficiently well matched to the data (see § 4.2.1).

^bNote that the PA is for the thinnest region of function.

^cThis is the near-to-far flux ratio (see §4.2.3).

Table 3. Comparison of Observed & Modeled Disk Properties ^a

	Data		Models			
	This paper	R96	This paper model 1	This paper model 2	Wood ^b <i>no CS disks</i>	Wood ^b <i>CS disks</i>
$R_{M_{F110W}}$	0.014 ± 0.0003	0.0043 ± 0.0012	0.007	0.012	0.030	0.008
$\Delta(M_{F110W} - M_{F160W})$	0.10 ± 0.03	0.65 ± 0.32	0.50	0.47	-0.07	-0.31
$\Delta(M_{F160W} - M_{F205W})$	-0.04 ± 0.06	-0.34 ± 0.45	0.28	0.20	-0.21	-0.20
$N_{F_{F110W}}^c$	1.41 ± 0.03	3.6 ± 1	1.90	2.35	0.67	4.11
$N_{F_{F160W}}$	1.39 ± 0.02	2.6 ± 0.25	1.82	2.03	0.67	4.07
$N_{F_{F205W}}$...	1.5 ± 0.5	1.70	1.741	0.67	3.65

^aNote that the R96 and Wood et al. (1999) results are based on ground-based JHK filter observations, which differ slightly from the NICMOS filters used here (see §2 for details).

^bWood et al. 1999 model 1 (no CS disks) and model 3 (CS disks) results, from their Table 3.

^cIntegrated flux from the ‘near’ side of the disk (180° section centered on northern-most part of the disk semi-minor axis), divided by that from the ‘far’ side (180° section centered on southern-most part of the disk semi-minor axis).

Table 4. Model Dust Grain Properties^a

λ (μm)	This paper		Wood	
	ω	g	ω	g
1.03	0.47	0.85
1.25	0.44	0.79	0.46	0.32
1.55	0.40	0.74
1.6	0.39	0.73	0.42	0.29
1.9	0.35	0.69
2.2	0.31	0.64	0.35	0.25

^aValues in bold represent those used to compare the NICMOS observations.

Fig. 1.— Models of the central binary, generated through PSF fitting, have been subtracted from the F110W, F160W and F205W images of the GG Tau system, revealing the large circumbinary ring. The images here show the central $\sim 5''$ region around the binary system GG Tau A, with North up and East to the left.

Fig. 2.— Radial plots of detected disk emission and estimated biases and uncertainties are shown. The first row plots the surface brightness azimuthal averages of the disk light (diamonds) and bias measurements (crosses; see section §3.2.2). The second row shows the azimuthal averages for the 1σ measurement uncertainty surface brightness (diamonds), and the statistical error associated with the bias estimates (crosses). The last row shows the resulting signal to noise for each filter, calculated using equations (1) and (2). The circumbinary disk is clearly detected at radii greater than $1''$, but the low SNR at radii less than $\sim 0.8''$ make detection of material in the disk gap impossible.

Fig. 3.— The GG Tau orbit, projected onto the plane of the sky. The dashed line corresponds to the line of nodes: the arrow on the right hand node denotes the ascending node, and hence the direction of orbital motion. Periastron and apoastron are marked. Overplotted on the orbit is the measured offset of the secondary from GG Tau Aa for seasonal averages of all the published data on this system, where observations from October through January of the next year are considered to be in the same season. These data points are connected to their corresponding modeled positions by thin lines.

Fig. 4.— The measured disk width, in arcseconds, per 10 degree sector, as a function of position angle on the sky for the F110W and F160W data.

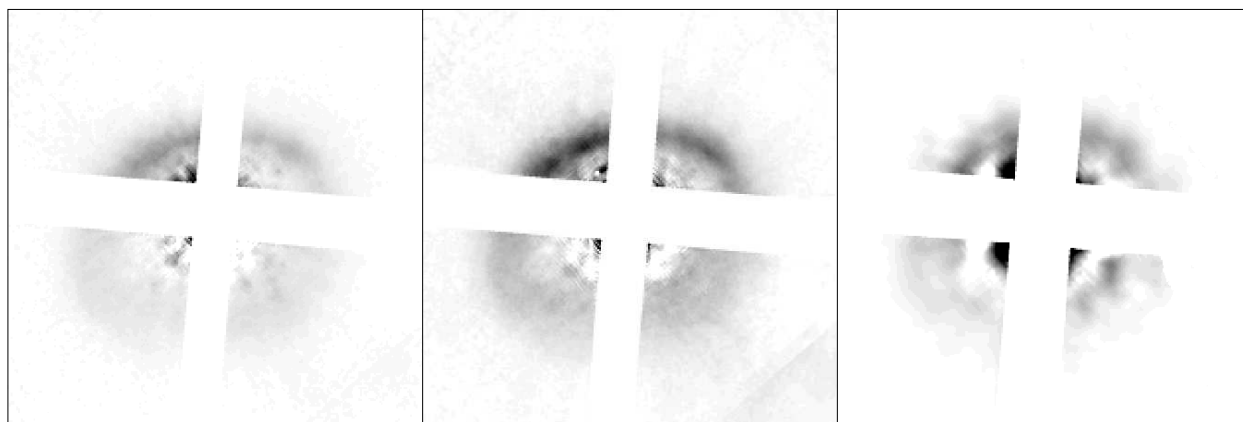
Fig. 5.— The F160W image of the disk, shown in contour levels set at 8%, 16%, 42%, 58% and 83% of the disk maximum. The kink in the disk is evident in the south-east quadrant of the disk where the contours turn sharply, creating an 'elbow' in the disk, and then flatten off along the southern edge of the disk.

Fig. 6.— Variations in color across the disk are investigated by calculating the magnitude in 9 pixel wide apertures placed within the disk photometric aperture. The $F110W - F160W$ color-magnitude diagram show no obvious color variations around the disk.

Fig. 7.— (*left*) Normalized disk peak flux per 10 degree sector, as a function of position angle on the sky for the F110W and F160W data. The Henyey-Greenstein scattering phase functions which maximize the disk intensity variations are shown (solid lines). The values of PA_0 found from the fitting process can be found in Table 2. (*right*) The observed azimuthal flux variation translated into a scattering phase function. The scattering phase function is symmetric around 180° and we therefore only show the $0 \rightarrow 180$ degree range. The best fitting

Heney-Greenstein scattering phase function for each filter is also shown (solid line), with $g = 0.39$ and 0.30 at $1.03 \mu\text{m}$ and $1.55 \mu\text{m}$ respectively.

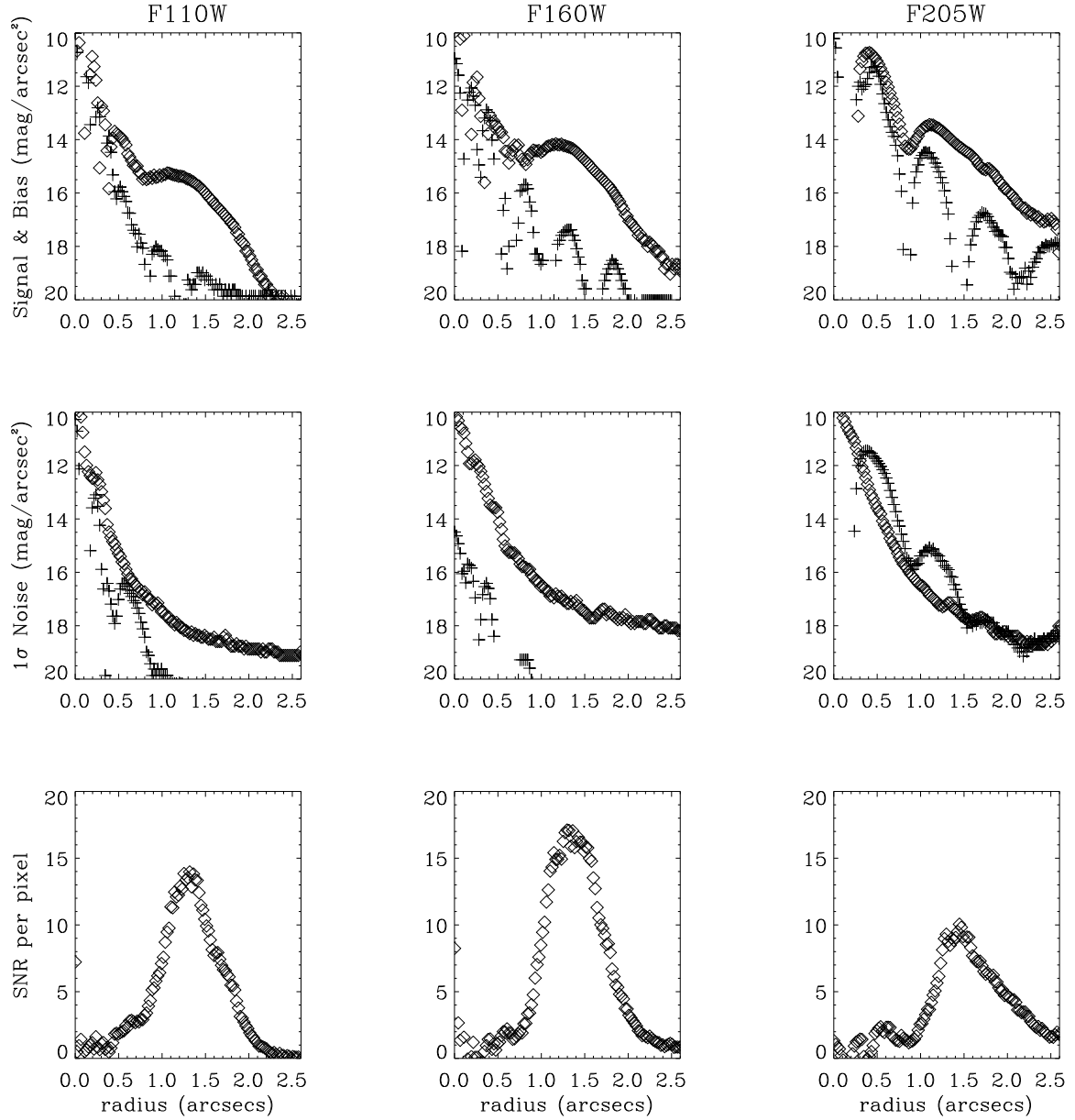
Fig. 8.— A cartoon of the disk showing (*left*) an on-sky view with the defined elliptical axes and position angle and (*right*) a side-view showing the relation between scattering angle, opening angle and disk geometry.

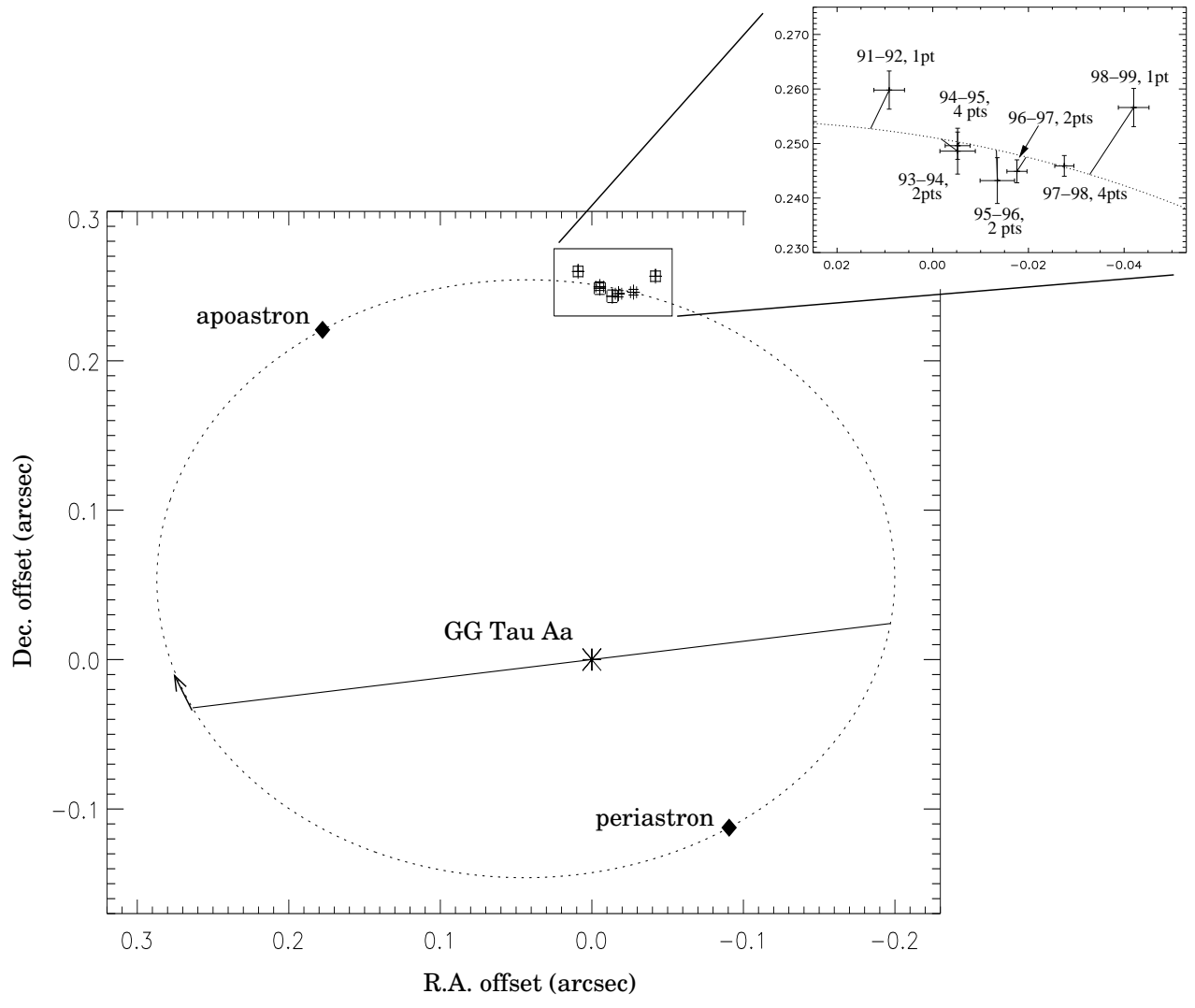


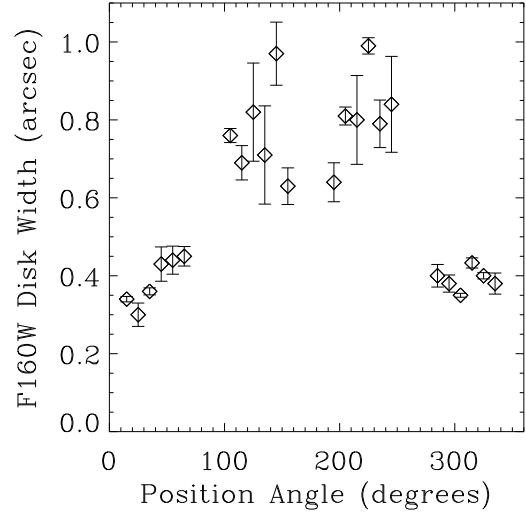
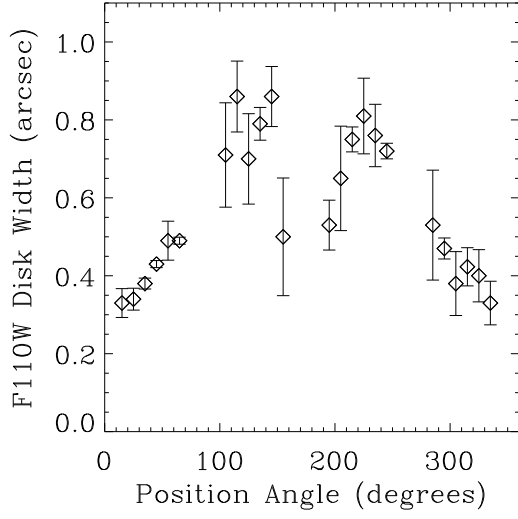
F110W

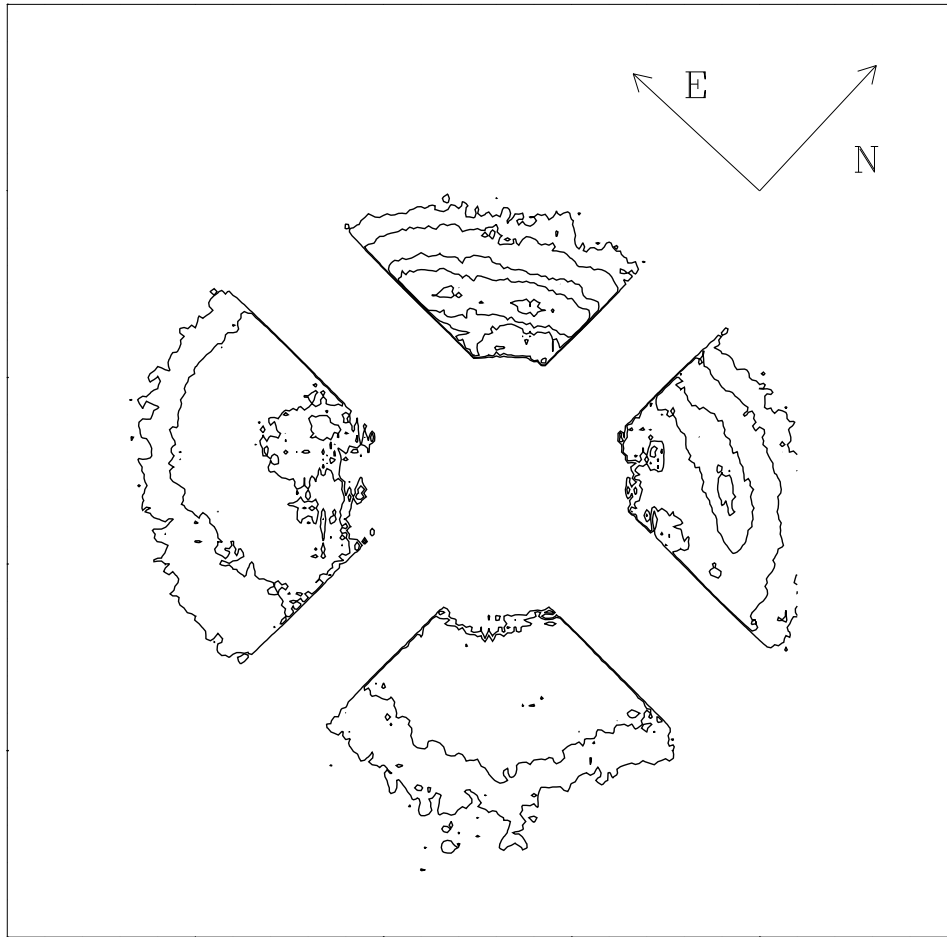
F160W

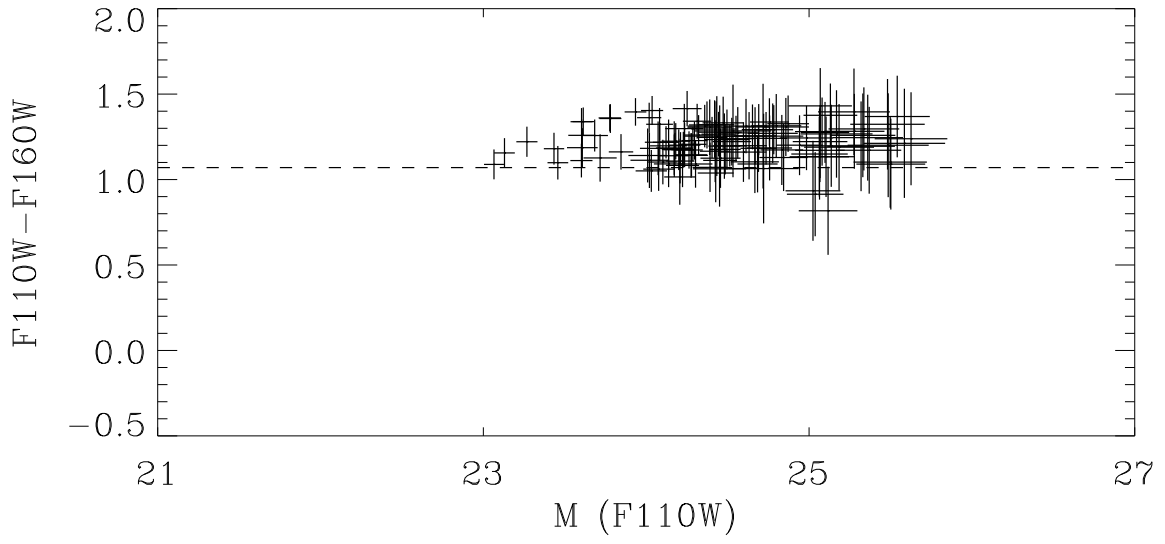
F205W



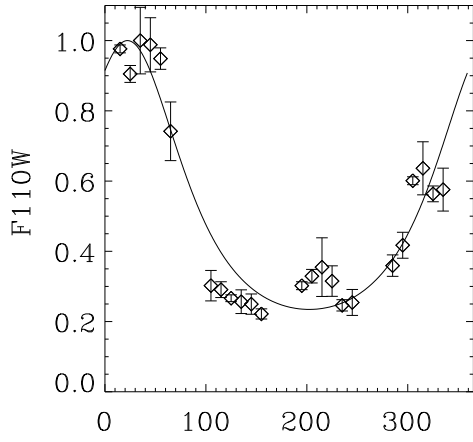




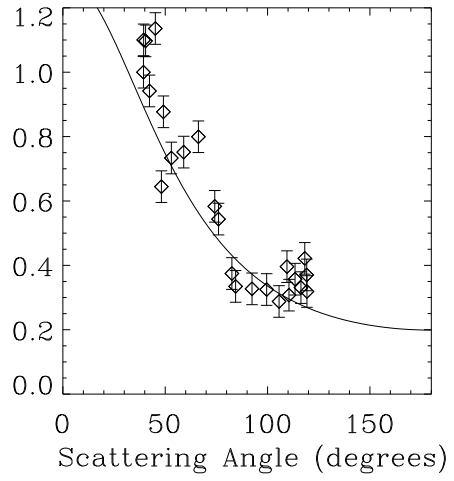
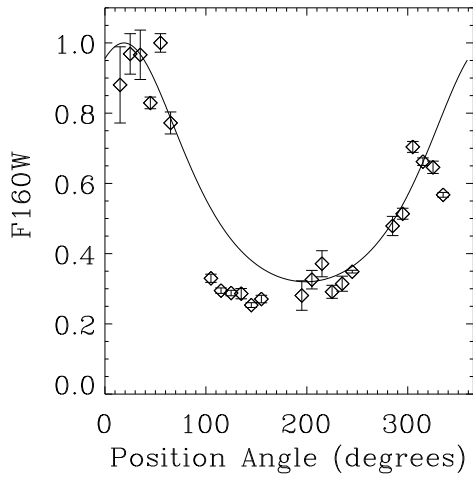
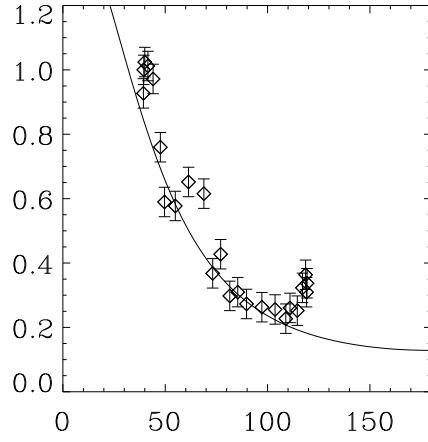


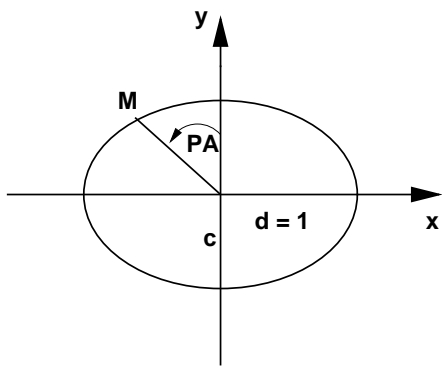


Normalized Peak Intensity

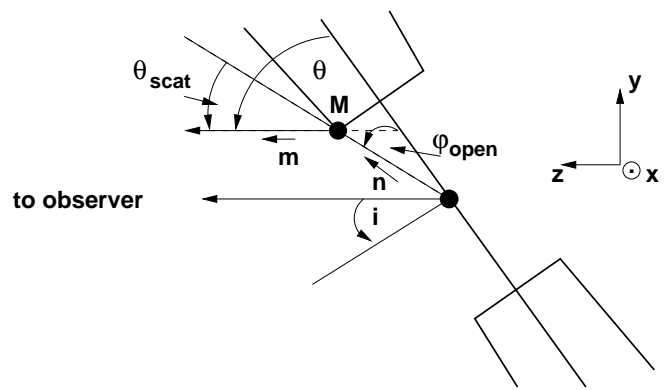


Deprojected Phase Function





ON SKY



SIDE VIEW